Journal of Colloid and Interface Science 686 (2025) 681–690

Contents lists available at ScienceDirect

Journal of Colloid And Interface Science

journal homepage: www.elsevier.com/locate/jcis

Regular Article

Enhancing hydrogen evolution by heterointerface engineering of Ni/MoN catalysts

Junzheng Jiang [a], Yunfan Qiu [a], Hao Dong [a], Lei Yang [b], Yaping Miao [c], Liwei Xiong [a], Biao Gao [d], Xuming Zhang [d], Paul K. Chu [e], Xiang Peng [a,*]

[a] Hubei Key Laboratory of Plasma Chemistry and Advanced Materials, Engineering Research Center of Phosphorus Resources Development and Utilization of Ministry of Education, School of Materials Science and Engineering, Wuhan Institute of Technology, Wuhan 430205 China
[b] Research Center for Monitoring and Environmental Sciences, Taihu Basin & East China Sea Ecological Environment Supervision and Administration Authority, Ministry of Ecology and Environment, Shanghai 200125 China
[c] School of Textile Science and Engineering, Xi'an Polytechnic University, Xi'an 710048 China
[d] The State Key Laboratory of Refractories and Metallurgy, Institute of Advanced Materials and Nanotechnology, Wuhan University of Science and Technology, Wuhan 430081 China
[e] Department of Physics, Department of Materials Science and Engineering, and Department of Biomedical Engineering, City University of Hong Kong, Tat Chee Avenue, Kowloon, Hong Kong, China

HIGHLIGHTS

- A programmed nitridation protocol is used to create Ni/MoN heterointerface.
- *In situ* phase separation induces electronic interaction between Ni and Mo atoms.
- Electron transfer from MoN to metallic Ni to generate a built-in electric field.
- The catalyst needs an overpotential of 95 mV for a current density of 10 mA cm^{-2}.
- The catalyst shows no morphology or composition changes at 100 mA cm^{-2} for 100 h.

GRAPHICAL ABSTRACT

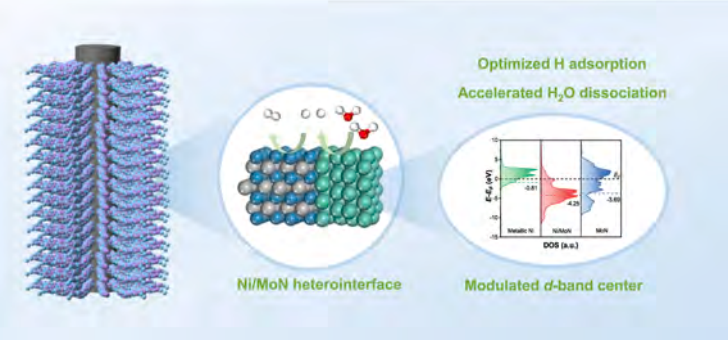

ARTICLE INFO

Keywords:
Heterointerface
Electronic interactions
Built-in electric field
Hydrogen evolution reaction
Water splitting

ABSTRACT

Molybdenum nitrides have garnered significant attention for their potential in the hydrogen evolution reaction (HER) due to their metallic behavior, abundant reserves, and pH-universal stability. However, their unsatisfactory hydrogen adsorption limits industrial applications. Heterostructures can be designed to introduce defects and modulate the electronic structure of catalysts to optimize hydrogen adsorption to enhance HER. Nevertheless, the exact active sites at the heterointerface and the fundamental mechanisms underlying the HER process remain inadequately understood. Herein, a composite electrocatalyst in which metallic Ni and MoN phases (Ni/MoN) form the heterointerface between them is fabricated. The heterointerface produces strong electronic interactions between Ni and MoN to facilitate electron transfer from MoN to Ni, and the built-in electric field facilitates charge transfer during electrocatalysis. This optimized electronic configuration with abundant active

* Corresponding author.
E-mail address: xpeng@wit.edu.cn (X. Peng).

https://doi.org/10.1016/j.jcis.2025.01.201
Received 2 December 2024; Received in revised form 8 January 2025; Accepted 23 January 2025
Available online 28 January 2025

sites delivers excellent performance in alkaline HER. Density-functional theory calculations demonstrate that H_2O dissociates at the Ni site, whereas H_2 desorption occurs at the Mo site. As a result, Ni/MoN/CC requires an overpotential of only 95 mV to achieve a current density of 10 mA cm^{-2} and a Tafel slope of 104 mV dec^{-1}. Moreover, it maintains a high current density of 100 mA cm^{-2} for 100 h with negligible morphological or compositional changes. The strategy of modulating the electronic structure of low-cost, transition metal-based heterostructured electrocatalysts is an effective and commercially viable means to design and develop high-performance electrocatalysts for water splitting.

1. Introduction

Hydrogen, which possesses a superior energy density compared to fossil fuels, chemical fuels, and biofuels, is recognized to be a clean and carbon-free energy source for renewable energy generation [1–3]. Clean hydrogen can be produced by green techniques such as water splitting [4–6]. Electrocatalysts containing noble metals like platinum and palladium are commonly used in the hydrogen evolution reaction (HER), but the high cost and natural scarcity have hampered more widespread industrial implementation [7–9]. Hence, it is crucial to develop more economical, abundant, and efficient electrocatalysts for water splitting in the pursuit of zero carbon emission.

Mo-based catalysts have been investigated for HER on account of their cost effectiveness, abundant reserves, and stability under different pH conditions [10,11]. In particular, Mo-based nitride (Mo_xN_y) has distinctive metallic properties and high corrosion resistance suitable for water splitting [12–17]. Ma et al. [18] have developed a composite of MoN and graphene (MoN/G) for HER. Graphene not only serves as a diffusion barrier to hinder the growth of two-dimensional (2D) MoN, but also improves charge transport in the heterogeneous structure. Consequently, the MoN/G heterostructure exhibits overpotentials of 155 mV and 259 mV for a current density of 10 mA cm^{-2} in 0.5 M H_2SO_4 and 1.0 M KOH, respectively. Xiong et al. [19] have proposed the synthesis of defective-rich molybdenum nitride (dr-MoN) nanosheets with a 2D structure with high efficiency in HER. In 0.5 M H_2SO_4 and 1.0 M KOH electrolytes, overpotentials of 125 mV and 139 mV are required to attain a current density of 10 mA cm^{-2}. Although defects in the structure give rise to minute cracks on the surface to expose additional edge sites, the HER activity of MoN is plagued by sluggish hydrogen desorption arising from strong Mo-H bonding [20].

The construction of heterostructures is an effective approach to enhance the properties of HER catalysts [21–23]. Heterointerfaces often exhibit defects and lattice disorder, which can be exploited to modulate the electronic structure of catalysts and optimize hydrogen adsorption [24–26]. Heterostructures composed of transition metal nitrides such as Co-Ni_3N [27], V-Co_4N [28], Cr-Co_4N [29], Co/MoN [30], and Co-Mo_5N_6 [31] have been shown to deliver comparable or even superior HER performance compared to the commercial Pt/C catalyst [32,33]. For instance, Zhao et al. [34] have designed N-doped CoMo MOFs-derived carbon nanospheres (Co/Mo-N) for HER. Since Co-N and Mo-N create rapid electron transfer pathways to enhance intermediate adsorption, the Co/Mo-N catalyst requires an overpotential of only 112 mV to achieve a current density of 10 mA cm^{-2} in 1.0 M KOH. Metallic Ni has good electrical conductivity and acts as an active HER site, but strong hydrogen adsorption poses limitations in practice [35]. Combining MoN with Ni to form a Ni/MoN heterostructure, in which the electronic structure of catalysts can be modified *via* defects and lattice disorder, can, in principle, optimize hydrogen adsorption and boost the electrocatalytic activity [36]. Nevertheless, the interactions between Mo-based nitride and Ni metal, as well as the underlying mechanism in HER, are not well understood [37,38].

Herein, a composite catalyst, Ni/MoN/CC with metallic Ni and MoN on carbon cloth (CC), is synthesized by a hydrothermal reaction followed by *in situ* phase separation, as illustrated in Scheme 1. The excellent electrical conductivity of both Ni and MoN components fosters rapid charge transfer during the electrochemical process. Furthermore, a strong electronic interaction is observed at the heterointerface between Ni and Mo, resulting in the transfer of electrons from MoN to metallic Ni and the formation of a built-in electric field. The electronic interaction modulates the electron configuration of the surface-active sites, promotes the dissociation of water, and optimizes hydrogen desorption. Theoretical calculations indicate that H_2O dissociates at the Ni sites, whereas H_2 desorption occurs at the Mo sites. Consequently, the Ni/MoN/CC catalyst has remarkable alkaline HER activity, such as an overpotential of only 95 mV to achieve a current density of 10 mA cm^{-2} in conjunction with a Tafel slope of 104 mV dec^{-1}. More importantly, the durability of Ni/MoN/CC is outstanding, as demonstrated by a constant current density of 100 mA cm^{-2} during continuous operation

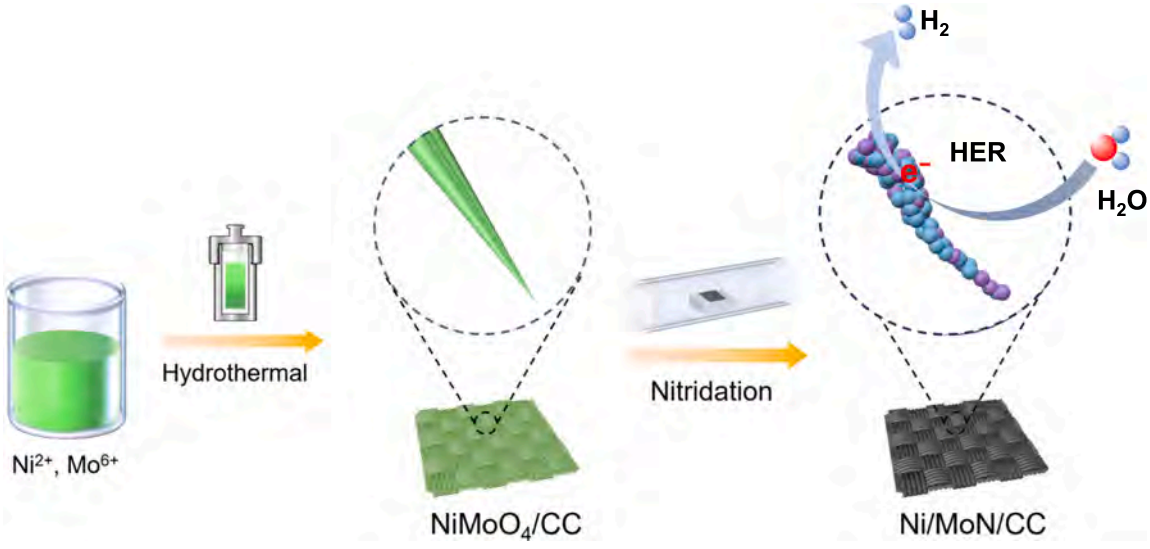

Scheme 1. Synthesis of the Ni/MoN heterostructure on CC and application to alkaline HER.

for 100 h.

2. Experimental details

2.1. Chemicals and materials

Nickel chloride hexahydrate ($NiCl_2{\cdot}6H_2O$, 99%, Macklin reagent), nickel sulfate hexahydrate ($NiSO_4{\cdot}6H_2O$, 99%, Macklin reagent), platinum carbon (Pt/C, nominally 20% on carbon black, Aladdin), and Nafion 117 (5%, Macklin reagent) were used directly without further purification. Sodium molybdate dihydrate ($Na_2MoO_4{\cdot}2H_2O$, AR), potassium hydroxide (KOH, AR), and concentrated sulfuric acid (H_2SO_4, AR) were purchased from Sinopharm. The deionized water (DW) used in this study had a resistivity of 18.25 MΩ cm^{-1} and was produced by an ultrapure cation system.

2.2. Materials preparation

The $NiMoO_4$ nanowires were synthesized on carbon cloth using a hydrothermal reaction. In brief, 1.5 mmol of nickel chloride hexahydrate ($NiCl_2{\cdot}6H_2O$) and 1.5 mmol of sodium molybdate dihydrate ($Na_2MoO_4{\cdot}2H_2O$) were dissolved in 30 mL of deionized water (DW) and stirred. The solution was transferred to a 50 mL Teflon-lined stainless-steel autoclave in which a piece of clean CC was positioned vertically and fully immersed in the solution. After reacting at 130°C for 6 h, the CC was taken out, washed with distilled water (DW), and dried at 60 °C overnight to form $NiMoO_4$/CC.

The $NiMoO_4$/CC was calcinated at 600 °C for 2 h under ammonia to obtain the composite containing metallic Ni and MoN on CC, denoted as Ni/MoN/CC. To prepare MoN/CC, the Ni/MoN/CC composite was immersed in 0.5 M H_2SO_4 at 50 °C for 30 min, leading to the dissolution of metallic Ni and the formation of MoN/CC. For comparison, Ni/CC was prepared by a hydrothermal reaction and ammonia calcination at 700 °C, but without the molybdenum source ($Na_2MoO_4{\cdot}2H_2O$).

2.3. Materials characterization

The morphology of the samples was examined by scanning electron microscopy (FE-SEM, TESCAN MIRA4), transmission electron microscopy (TEM, FEI Tecnai G2 F30), and energy-dispersive X-ray spectroscopy (EDS). The structure of the samples was determined by X-ray diffraction (XRD, LabX XRD-6100, Shimadzu) and high-resolution TEM (HR-TEM). The chemical states were determined by X-ray photoelectron spectroscopy (XPS, Thermo Scientific *K*-Alpha, ThermoFisher) with monochromatic Al K_α X-ray.

2.4. Electrochemical evaluation

The electrochemical experiments were conducted using a typical three-electrode configuration in a 1.0 M KOH electrolyte on an electrochemical workstation (CHI 660E, Shanghai CH Instruments, China). The working electrode consisted of CC modified with the catalyst, with Hg/HgO as the reference electrode and a graphite rod as the counter electrode. All the potentials were 100 % *iR* corrected and calibrated to the reversible hydrogen electrode (RHE) according to the Nernst equation $E_{RHE} = E_{Hg/HgO} + 0.098 + 0.059pH$. The pH of the 1.0 M KOH solution was determined to be 13.80 by a pH meter (FE28, Mettler Toledo). The current densities were calculated based on the geometric surface area on the electrodes. Linear scanning voltammetry (LSV) was employed to obtain the polarization curves at a scanning rate of 5 mV s^{-1}. The Tafel slopes, represented by overpotentials (η) plotted against logarithmic currents ($\log|j|$), were derived from the polarization curves. To determine the electrochemically active surface area (ECSA), a series of cyclic voltammetry (CV) experiments were performed in the potential range from −0.4 to −0.5 V *vs.* the Hg/HgO electrode at scanning rates between 10 and 100 mV s^{-1}. Electrochemical impedance spectroscopy (EIS) was conducted at an initial potential of −1.2 V *vs* Hg/HgO with an amplitude of 5 mV between 100 kHz and 0.1 Hz. The stability was assessed by applying a constant current density for 100 h.

2.5. Density-functional theory calculations

Density-functional theory (DFT) calculations were performed based on first principles. The results were obtained by generalized gradient approximation (GGA) with the PBE exchange–correlation functional and a cutoff energy of 500 eV. All the calculations were van der Waals corrected with DFT-D. A 1 × 1 × 1 *k*-point grid was used to sample the Brillouin zone in the models. The lattice parameters of the model of Ni/MoN were a = 8.53 Å, b = 17.22 Å, c = 37.26 Å, with all angles being 90°. The vacuum layer thickness was 15 Å. In the iterative solution of the Kohn-Sham equations, the energy convergence criterion was set to be 10^{-5} eV, and the forces on each atom were converged to within 0.02 eV/Å. The hydrogen adsorption free energy was calculated as shown in the following:

$$\Delta E_{H^*} = E_{(slab+H^*)} + E_{(slab)} + 1/2E_{H_2} \quad (1)$$

$$\Delta G_{H^*} = \Delta E_{H^*} + \Delta E_{ZPE} - T\Delta S \quad (2)$$

where ΔE_{H^*} represents the adsorption energy of H, $\Delta E_{(slab\ +\ H^*)}$ is the total energy of H on the catalyst surface, $\Delta E_{(slab)}$ and ΔE_{H2} are the total energies of the catalyst and H_2, respectively, ΔG_{H^*} is the hydrogen adsorption free energy, and ΔE_{ZPE} and $T\Delta S$ represent the zero-point energy and vibrational energy, respectively. According to the study by Nørskov et al. [39], $\Delta E_{ZPE} - T\Delta S$ is considered to be 0.24 eV.

3. Results and discussion

The synthesis process of the Ni/MoN/CC electrocatalyst is illustrated in Scheme 1. The $NiMoO_4$ nanowire arrays are prepared on CC hydrothermally. Subsequently, a programmed nitriding procedure is carried out in an ammonia atmosphere to separate the Ni and Mo species in $NiMoO_4$ and form the metallic Ni and MoN heterostructure on the CC framework (Ni/MoN/CC). Previous studies have unveiled that Ni_3N is unstable at a high temperature, and nitrogen atoms easily detach from the Ni_3N lattice, leading to the formation of metallic Ni [40,41]. The heterostructure between these two phases produces strong electronic interactions to activate the surface atoms for accelerated electrocatalysis.

Fig. 1**a** depicts the morphological evolution from $NiMoO_4$/CC to Ni/MoN/CC during ammonia nitridation. The O atoms in $NiMoO_4$ are replaced by N atoms, resulting in a decrease in the total number of atoms. Consequently, a porous structure is generated, accompanied by volume shrinkage [42]. The $NiMoO_4$ nanowire arrays on CC have a smooth surface, as shown in Fig. 1**b-c**. After nitriding at 600 °C in ammonia, the nanowire array structure remains, but the surface consisting of nanoparticles becomes porous, as depicted in Fig. 1**d-e**. Moreover, the straight nanowires are bent due to the escape of the oxygen atoms, giving rise to volume shrinking. The rough surface on Ni/MoN/CC exposes a larger specific surface area for the catalytic activity [43,44]. **Fig. S1** shows that MoN/CC is uniformly distributed on CC while exhibiting a curved nanowire structure with a rough surface composed of nanoparticles. **Fig. S2** indicates that Ni/CC is distributed on CC in the form of spherical particles.

Fig. 2**a** shows the morphology of Ni/MoN on CC with a nanowire diameter of approximately 70 nm and with a large number of attached nanoparticles consistent with SEM. HR-TEM image in Fig. 2**b** shows that the interplanar spacings of the lattice fringes are 0.248 and 0.203 nm, corresponding to the MoN (200) and metallic Ni (1 1 1) planes, respectively. The heterointerface between MoN and metallic Ni phases is clearly discernible and expected to modulate the electronic structure of the interfacial atoms [45]. The selected-area electron diffraction (SAED)

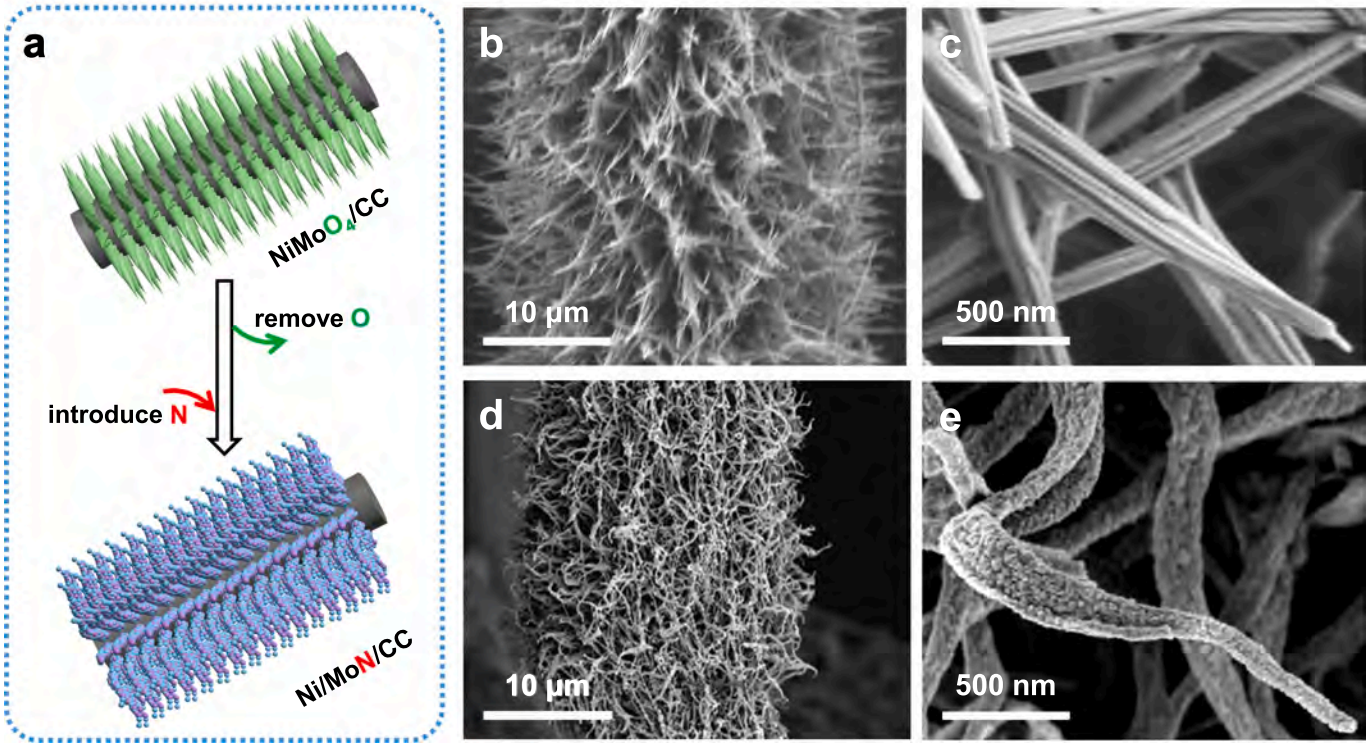

Fig. 1. (a) Schematic illustration of the morphological evolution from $NiMoO_4$/CC to Ni/MoN/CC; SEM images of (b-c) $NiMoO_4$/CC and (d-e) Ni/MoN/CC.

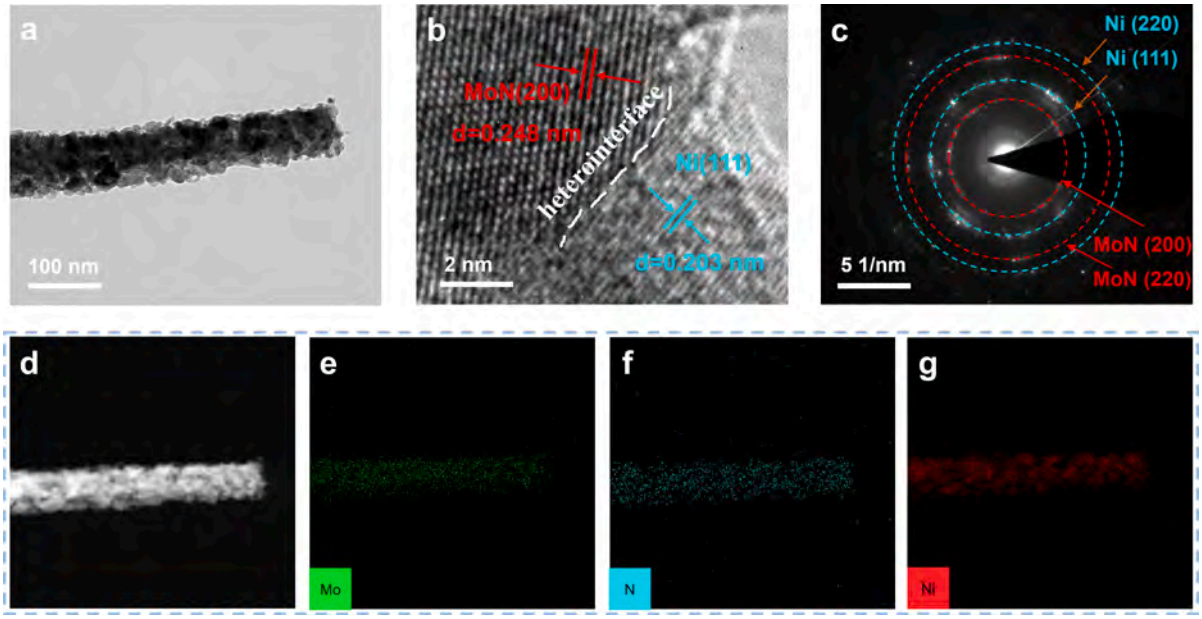

Fig. 2. (a) TEM image, (b) HR-TEM image, and (c) SAED pattern of Ni/MoN; (d-g) Elemental maps of Mo, N, and Ni in Ni/MoN.

pattern in Fig. 2**c** shows the (1 1 1) and (220) facets of metallic Ni as well as (200) and (220) facets of MoN, implying a mixed composition of Ni and MoN. The elemental maps in Fig. 2**d-g** confirm uniform distributions of Mo, N, and Ni in Ni/MoN/CC.

Fig. S3 displays the XRD pattern of the hydrothermal product, which matches well that of $NiMoO_4$ (JCPDS card No. 45–0142) [46] and confirms the fabrication of $NiMoO_4$ nanowire arrays on CC. As shown in Fig. 3**a**, the diffraction peaks at 32.2°, 36.6°, 49.5°, 65.8°, and 86.7° after nitridation of the $NiMoO_4$/CC precursor can be indexed to the (002), (200), (202), (220), and (402) planes of the hexagonal phase MoN (JCPDS card No. 25–1367), respectively, while those at 44.4°, 51.8°, and 76.5° correspond to the (111), (200), and (220) planes of cubic phase metallic Ni (JCPDS card No. 04–0850). The results confirm the formation of the composite consisting of hexagonal phase MoN and cubic phase metal Ni after ammonia nitridation. The well-preserved nanowire structure after nitridation suggests the *in situ* separation of MoN and Ni from $NiMoO_4$ as well as the formation of a heterointerface between these two phases. Ensuing acid etching of Ni/MoN/CC results in a diffraction pattern (MoN/CC) that matches the hexagonal phase MoN (JCPDS card No. 25–1367), except a small diffraction peak at 43.6° attributable to

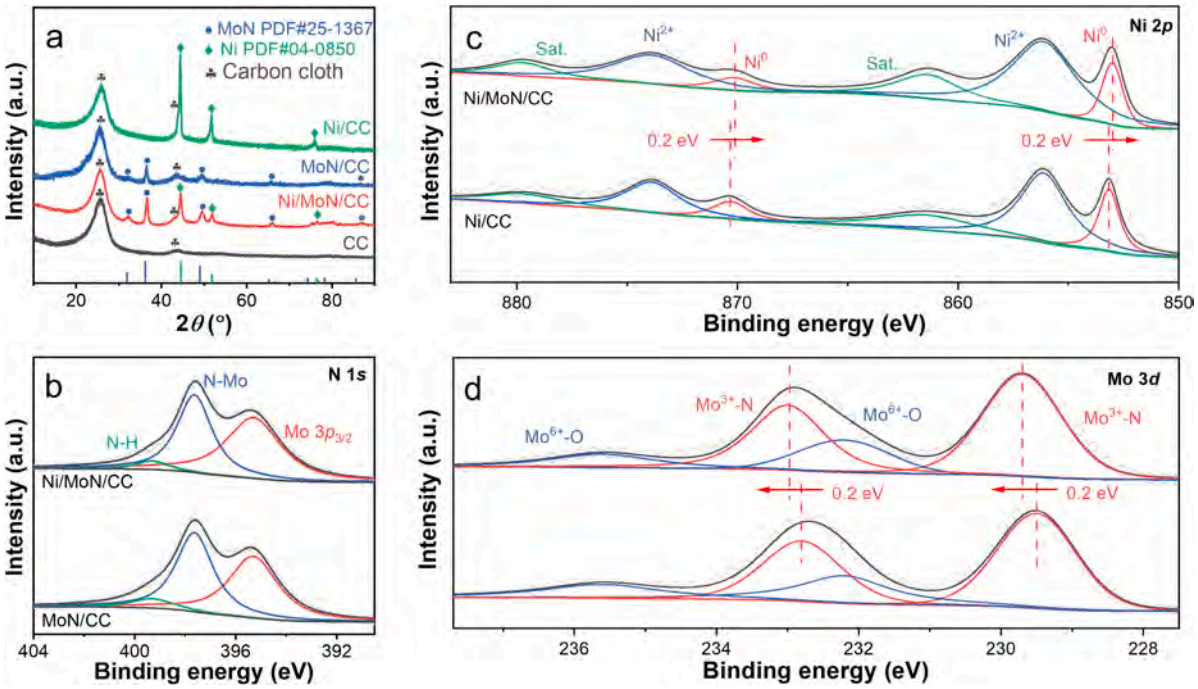

Fig. 3. XRD and XPS spectra of Ni/MoN/CC, MoN/CC, and Ni/CC: (a) XRD spectra, High-resolution XPS spectra of (b) N 1*s*, (c) Ni 2*p*, and (d) Mo 3*d*.

CC. The results corroborate the removal of metallic Ni from Ni/MoN/CC. The diffraction peaks of the sample prepared without the Mo source (Ni/CC) correspond to cubic metallic Ni (JCPDS card No. 04–0850), indicating the growth of pure-phase metallic Ni on CC.

Fig. 3**b** exhibits the XPS N 1*s* spectra of Ni/MoN/CC and MoN/CC. The peaks at 397.6 eV and 399.3 eV correspond to N-Mo and N—H, respectively [47]. The N—H species are generated by the decomposition of the NH_3 during heating [48]. The peak at 395.3 eV is associated with

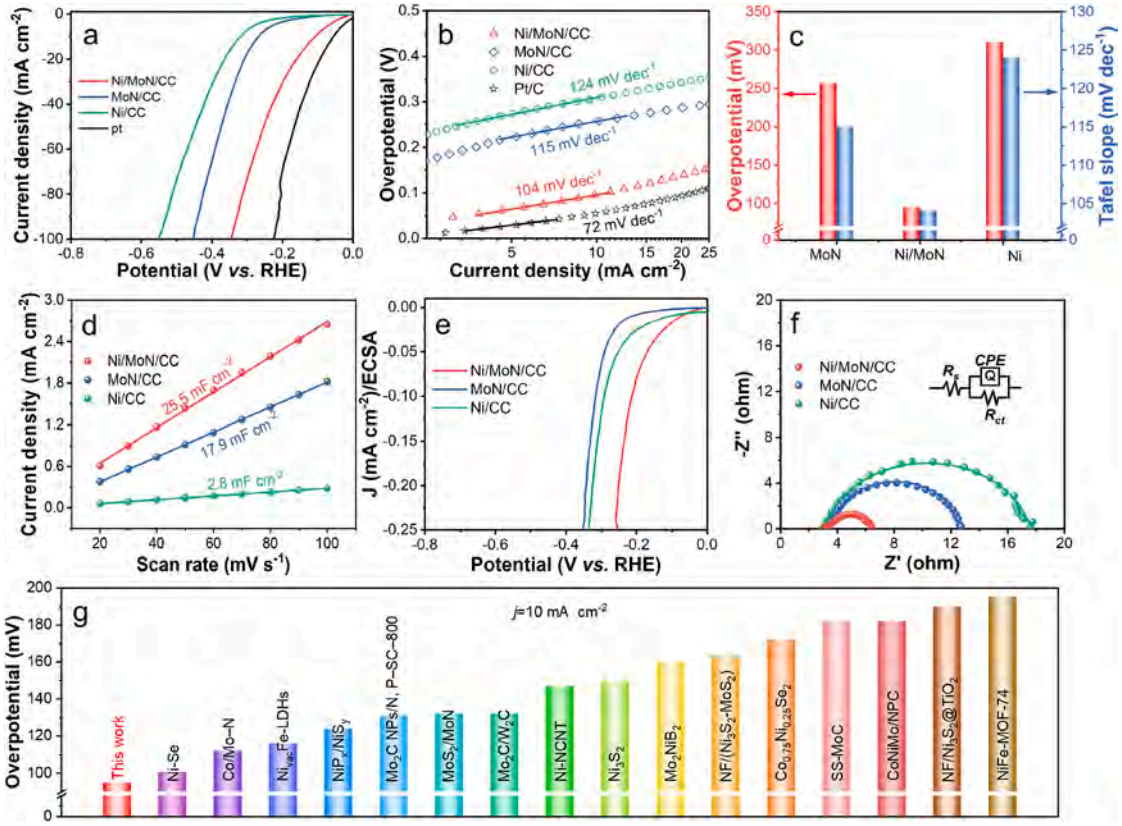

Fig. 4. Electrocatalytic properties of Ni/MoN/CC, MoN/CC, and Ni/CC. (a) LSV curves; (b) Tafel plots; (c) Overpotentials required for a current density of 10 mA cm^{-2} and Tafel slopes; (d) ECSA; (e) Normalized LSV curves based on ECSA; (f) EIS with the equivalent circuit in the inset; (g) Comparison of the as-prepared Ni/MoN/CC with other similar catalysts.

Mo-3$p_{3/2}$. The high-resolution XPS Ni 2*p* spectra of Ni/CC and Ni/MoN/CC in Fig. 3**c** indicate the presence of Ni^{2+} species at 856.2 eV and 873.9 eV. The Ni^{2+} species are produced by partial oxidation of the surface upon air exposure [49]. The peaks at 852.9 ~ 853.1 eV and 870.1 ~ 870.3 eV of Ni/MoN/CC and Ni/CC arise from Ni^0 species, confirming the presence of metallic Ni in both samples [50]. The binding energy of Ni^0 species in Ni/MoN/CC exhibits a negative shift of 0.2 eV compared to the pure phase of Ni/CC. Fig. 3**d** displays the high-resolution XPS Mo 3*d* spectra of MoN/CC and Ni/MoN/CC. The peaks at 229.5 ~ 229.7 eV and 232.7 ~ 232.9 eV are attributed to Mo-N species [51], and those at 232.2 eV and 235.6 eV arise from Mo^{6+}-O species due to slight oxidation in air [52]. Compared to the pure phase MoN/CC, the binding energy of Mo-N in Ni/MoN/CC exhibits a positive shift of 0.2 eV. These binding energy shifts suggest the formation of a heterointerface between the two phases (metallic Ni and MoN), through which electrons can flow from the MoN phase to the metallic Ni to create a built-in electric field that facilitates charge transfer during electrocatalysis [53].

The electrocatalytic properties are evaluated in a 1.0 M KOH. The potentials reported here are 100 % *iR*-corrected to evaluate the intrinsic activity of the catalysts. The uncorrected polarization curves are shown in **Fig. S4**. As shown by the polarization curves in Fig. 4**a**, Ni/MoN/CC shows lower overpotentials (95 mV for 10 mA cm^{-2} and 237 mV for 100 mA cm^{-2}) than MoN/CC (257 mV for 10 mA cm^{-2} and 346 mV for 100 mA cm^{-2}) and Ni/CC (310 mV for 10 mA cm^{-2} and 444 mV for 100 mA cm^{-2}), providing clue that the heterointerface between the metallic Ni and MoN phases in Ni/MoN/CC activates the surface atoms and enhances the intrinsic electrocatalytic activity. The Tafel slope of Ni/MoN/CC (104 mV dec^{-1}) is smaller than those of MoN/CC (115 mV dec^{-1}) and Ni/CC (124 mV dec^{-1}), as shown in Fig. 4**b**. The Tafel slope reflects the reaction kinetics in HER. The smaller Tafel slope of Ni/MoN/CC indicates faster reaction kinetics and superior HER activity compared to the pure phases of MoN/CC and Ni/CC. The overpotentials for a current density of 10 mA cm^{-2} and Tafel slopes are summarized in Fig. 4**c**. The turnover frequency (TOF) is used to evaluate the intrinsic activity of the catalyst. As shown in **Fig. S5**, Ni/MoN/CC exhibits a TOF of 0.2 s^{-1} at an overpotential of 325 mV, which is larger than those of other catalysts.

The ECSA is determined by the electrical double-layer capacitance (C_{dl}). The CV curves of the MoN/CC, Ni/MoN/CC, and Ni/CC are acquired from the non-Faradic region (**Fig. S6**) to derive C_{dl}. Ni/MoN/CC exhibits the largest C_{dl} of 25.5 mF cm^{-2}, followed by MoN/CC (17.9 mF cm^{-2}) and Ni/CC (2.8 mF cm^{-2}), as shown in Fig. 4**d**. A larger C_{dl} indicates more exposed active sites, and Ni/MoN/CC has a greater number of active sites for HER due to the rough surface of Ni/MoN and the heterointerface to activate the surface atoms. The ECSA-normalized LSV curves in Fig. 4**e** further highlight the excellent intrinsic HER activity of Ni/MoN/CC. The heterointerface between the metallic Ni and MoN phases activates the inner surface atoms to serve as active centers in HER, and the built-in electric field at the heterointerface further accelerates charge transfer. The interaction produces more active sites, enhanced intrinsic catalytic activity, and fast charge transfer to expedite HER [54,55].

The electrochemical impedance spectroscopy (EIS) results in Fig. 4**f** show a smaller charge transfer resistance for Ni/MoN/CC compared to the pure phases of MoN/CC and Ni/CC, implying faster HER kinetics. Fig. 4**g** compares the overpotentials required to achieve a current density of 10 mA cm^{-2}. The overpotential of Ni/MoN/CC (95 mV) is lower than those of other recently reported catalysts, including Ni-Se (100.7 mV) [56], N-Co/Mo-MOFs (112 mV) [34], Ni_{vac}Fe-LDHs (116 mV) [57], NiP_x/NiS_y (124 mV) [58], Mo_2C NPs/N, P-SC-800 (131 mV) [59], MoS_2/MoN (132 mV) [60], Mo_2C/W_2C (132 mV) [61], Ni-NCNT (147 mV) [62], Ni_3S_2 (150 mV) [58], Mo_2NiB_2 (160 mV) [63], NF/(Ni_3S_2-MoS_2) (164 mV) [64], $Co_{0.75}Ni_{0.25}Se_2$ (172 mV) [65], SS-MoC (182 mV) [66], CoNiMo/NPC (182 mV) [67], NF/Ni_3S_2@TiO_2 (190 mV) [64], and NiFe-MOF-74 (195 mV) [68]. This comparison demonstrates the excellent properties of Ni/MoN/CC as an electrocatalyst for HER.

Stability is an important factor in assessing the performance of a catalyst. Fig. 5**a** displays the chronopotentiometry plot of Ni/MoN/CC in 1.0 M KOH. The potential required for a current density of 100 mA cm^{-2} remains unchanged after continuous operation for 100 h. To further evaluate the durability of Ni/MoN/CC, Fig. 5**b** compares the LSV curves before and after the 100 h operation. The curves exhibit no significant change, even at a large current density of 100 mA cm^{-2}, demonstrating the superior durability of Ni/MoN/CC in alkaline HER.

The hydrogen production capability and Faraday efficiency (*FE*) of Ni/MoN/CC are determined. Fig. 5**c** illustrates the setup used to collect and measure electrocatalytically produced oxygen and hydrogen by the water displacement method. Within 60 min and at a current of 100 mA, 22.5 mL of oxygen and 45.0 mL of hydrogen were collected, as shown in Fig. 5**d**. The yields of hydrogen and oxygen are calculated to be 2.008 and 1.004 mmol h^{-1}, respectively. Moreover, an extremely high energy conversion efficiency of 98.7% is accomplished. The high *FE* arises from that the internal electric field generated at the heterogeneous interface facilitates electron transfer and enhances the intrinsic catalytic activity of the interfacial atoms, consequently giving rise to faster reaction kinetics.

After the stability test, the morphology, structure, and surface chemistry of the Ni/MoN/CC catalyst are analyzed. Fig. 6**a-b** shows that the porous and curved nanowire arrays are preserved after the long-term test, indicating robust structural stability. The XRD pattern in Fig. 6**c** confirms that the crystal structure and composition of Ni/MoN/CC do not change after the stability test, with the diffraction peaks corresponding to the hexagonal-phase MoN (JCPDS card No. 25–1367) and cubic-phase metallic Ni (JCPDS card No. 04–0850). The chemical states also do not change, as shown by the high-resolution XPS spectra of Ni 2*p*, Mo 3*d*, and N 1*s* in Fig. 6**d-f**. Although the intensity of Ni^0 diminishes slightly due to unavoidable surface oxidation, both the Mo 3*d* and N 1*s* spectra are the same as those of the pristine sample. These results corroborate the excellent structural stability and chemical durability of Ni/MoN/CC in alkaline HER.

DFT calculations are performed to elucidate the catalytic mechanism of Ni/MoN. The models of Ni, MoN, and Ni/MoN composed of Ni(111) and MoN(200) surfaces are constructed based on XRD and TEM, as shown in Figs. 7**a and S7**. The density of states (DOS) near the Fermi level is continuously distributed, suggesting that Ni/MoN is metallic and has good conductivity (Fig. 7**b**). The *d*-band centers of metallic Ni, MoN, and Ni/MoN are calculated to be − 0.81, −3.96 eV, and − 4.25 eV, respectively, as shown in Fig. 7**c**. The lower *d*-band center of the Ni/MoN heterostructure indicates that there are more anti-bonding orbitals below the Fermi level, thus reducing the bonding strength between H and Mo atoms and better H desorption [69,70].

In the alkaline environment, HER normally proceeds by the Volmer (H_2O dissociation)-Heyrovsky (H adsorption/desorption) route, resulting in a sluggish reaction rate [71]. Therefore, the water dissociation and hydrogen adsorption properties of Ni/MoN were investigated. Fig. 7**d** reveals that the dissociation energy of water at the Ni sites in Ni/MoN (0.41 eV) is lower than that at the Mo sites in Ni/MoN (0.46 eV). Conversely, ΔG_{H^*} at the Mo sites in Ni/MoN is − 0.485 eV and considerably closer to zero than that of the Ni sites in Ni/MoN (−0.77 eV). Consequently, Ni functions as the hydrolysis dissociation site while Mo acts as the hydrogen desorption site at the Ni/MoN heterointerface during alkaline HER. The DFT results provide evidence that the Ni/MoN heterojunction optimizes the electronic structure of Ni and Mo sites, promotes H_2O dissociation, and enhances hydrogen desorption. As a result, Ni/MoN exhibits excellent alkaline HER activity.

4. Conclusions

A composite electrocatalyst, Ni/MoN/CC consisting of metallic Ni and MoN phases with a heterointerface between them, is prepared by a hydrothermal process followed by *in situ* phase separation. The heterogeneous interface plays a crucial role in the strong electronic interactions between Ni and MoN, which enables electron transfer

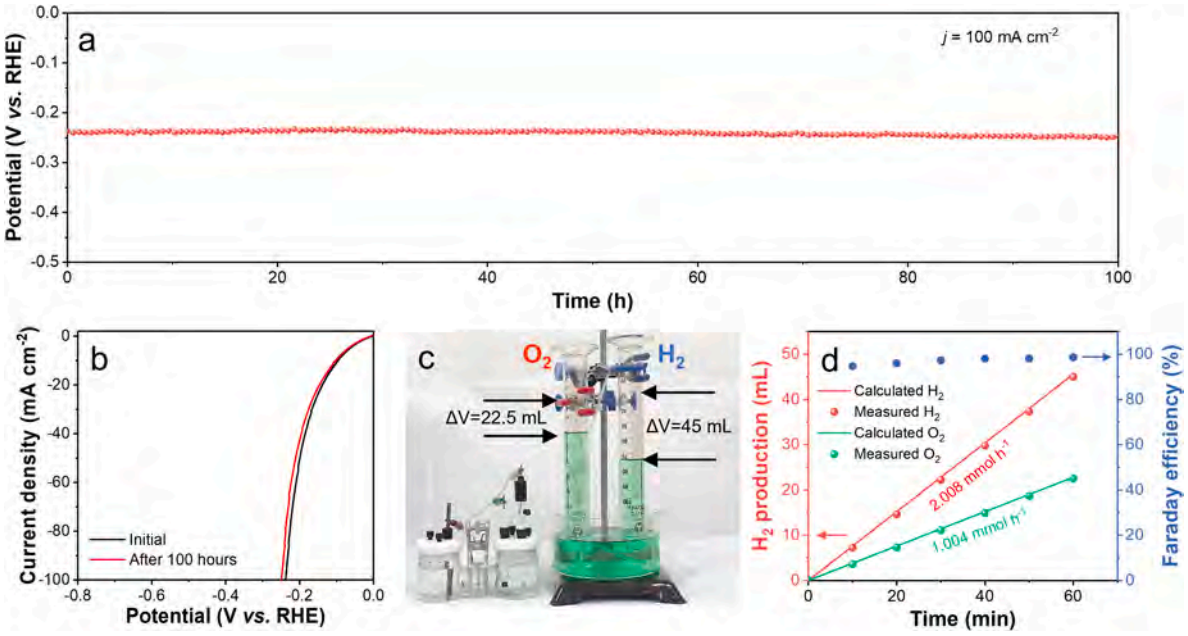

Fig. 5. Stability and H_2 production of Ni/MoN/CC. (a) Chronopotentiometry plot; (b) LSV curves before and after 100 h operation; (c) Illustration of the collection and volume determination of the amounts of H_2 and O_2 by the water displacement method; (d) Theoretically calculated and experimentally determined quantities of H_2 and O_2 as well as *FE* for hydrogen production at a current of 100 mA.

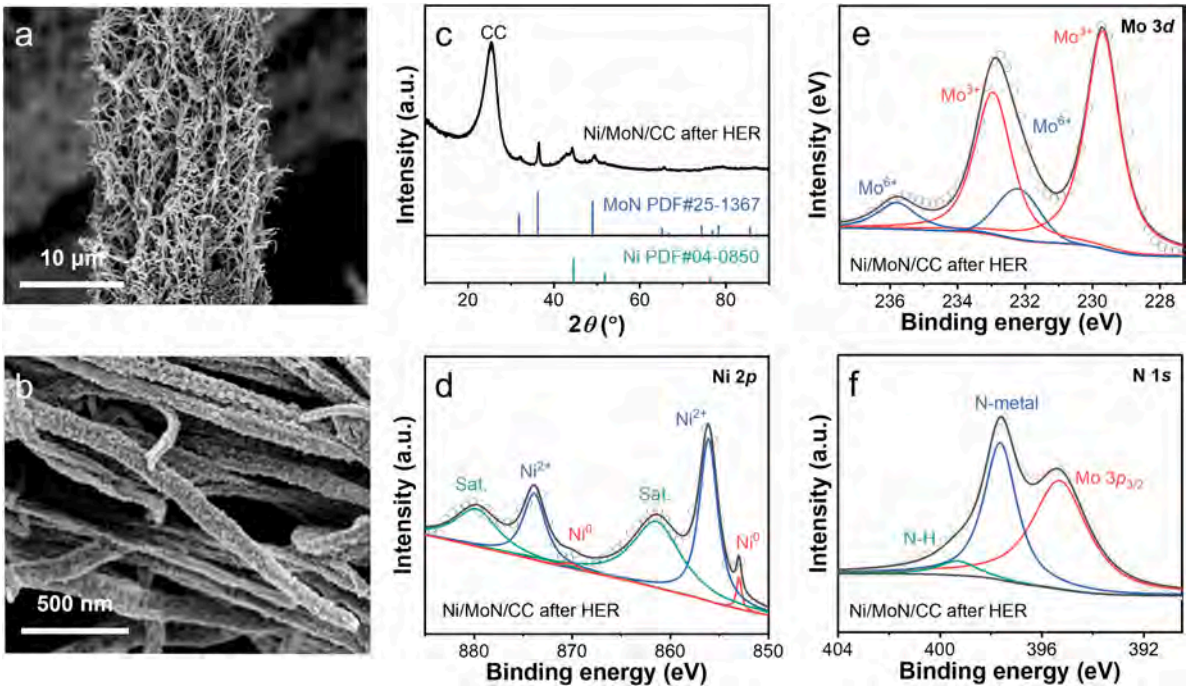

Fig. 6. Morphology and composition of Ni/MoN/CC after the stability test. (a, b) SEM images; (c) XRD spectrum; High-resolution XPS spectra of (d) Ni 2*p*, (e) Mo 3*d*, and (f) N 1 *s*.

between Ni and MoN and produce a built-in electric field to facilitate the dissociation of water and desorption of hydrogen in HER. DFT results indicate that H_2O dissociates at the Ni sites, whereas H_2 desorption occurs at the Mo sites. As a result, Ni/MoN/CC delivers remarkable electrocatalytic performance in alkaline HER. It requires a small overpotential of 95 mV to achieve a current density of 10 mA cm^{-2} with a Tafel slope of 104 mV dec^{-1}. More importantly, Ni/MoN/CC exhibits outstanding durability as demonstrated by insignificant morphological and compositional changes after continuous operation for 100 h at a large current density of 100 mA cm^{-2}. To assess the practical viability, Ni/MoN/CC shows a high hydrogen production yield of 2.008mmol h^{-1} and an impressive *FE* of 98.7%. The strategy of modulating the electronic structure of low-cost transition metal-based electrocatalysts is important to the design and development of high-performance catalysts for electrocatalytic water splitting.

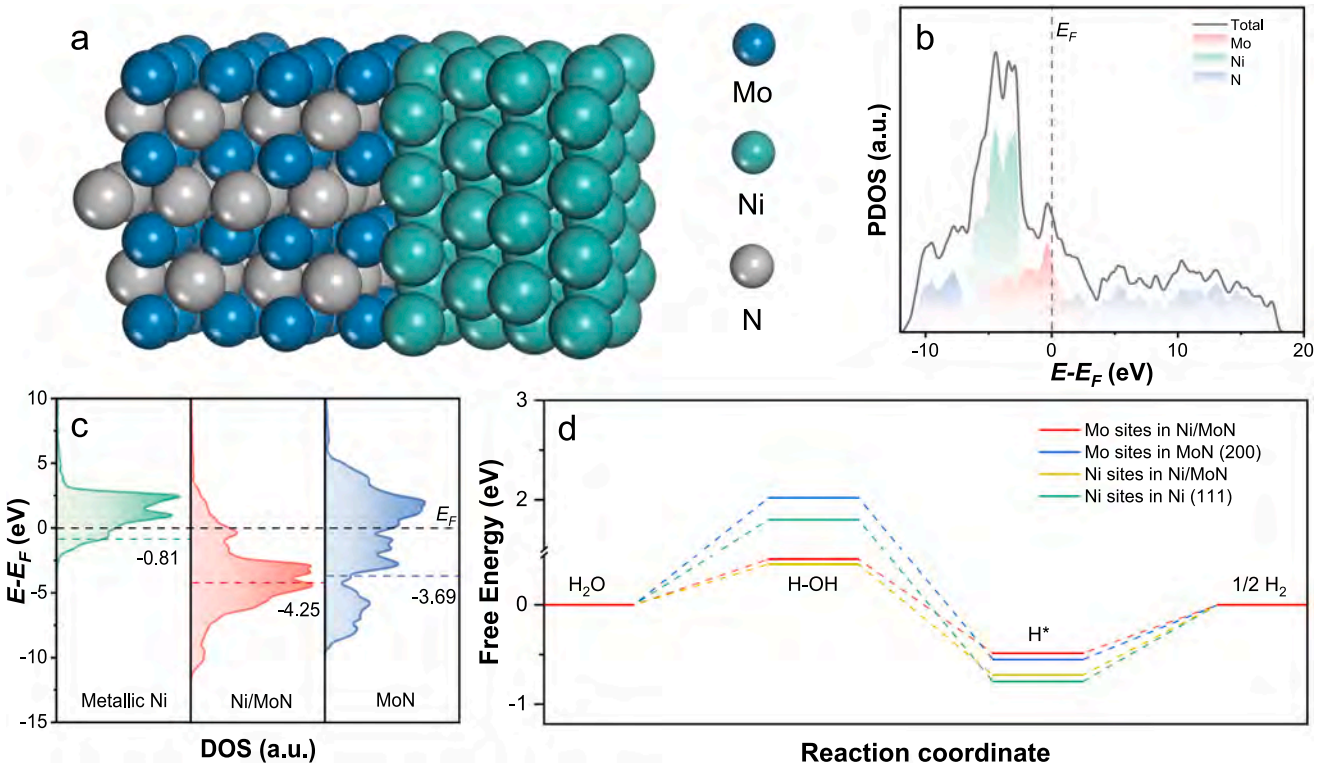

Fig. 7. (a) Optimized model for Ni/MoN heterojunction; (b) PDOS of the Ni/MoN heterojunction; (c) DOS of Ni (111), Ni/MoN, and MoN (200) showing the *d*-band centers; (d) H_2O dissociation energy and hydrogen adsorption free energy of the Ni/MoN heterojunction, MoN, and metallic Ni.

CRediT authorship contribution statement

Junzheng Jiang: Writing – review & editing, Writing – original draft, Visualization, Validation, Methodology, Investigation, Formal analysis, Data curation. **Yunfan Qiu:** Writing – review & editing, Writing – original draft, Methodology, Investigation, Formal analysis, Data curation. **Hao Dong:** Writing – review & editing, Validation, Methodology, Data curation. **Lei Yang:** Writing – review & editing, Validation, Methodology, Investigation. **Yaping Miao:** Writing – review & editing, Software, Resources, Formal analysis. **Liwei Xiong:** Writing – review & editing, Validation, Methodology, Formal analysis. **Biao Gao:** Writing – review & editing, Visualization, Resources. **Xuming Zhang:** Writing – review & editing, Validation, Methodology, Funding acquisition. **Paul K. Chu:** Writing – review & editing, Supervision, Funding acquisition. **Xiang Peng:** Writing – review & editing, Supervision, Project administration, Funding acquisition, Conceptualization.

Declaration of competing interest

The authors declare that they have no known competing financial interests or personal relationships that could have appeared to influence the work reported in this paper.

Acknowledgments

This work was financially supported by the National Natural Science Foundation of China (Nos. 52002294 and 22379116), Key Scientific Research Program of the Department of Education of Hubei Province (No. D20231501), and City University of Hong Kong Donation Research Grants (Nos. DON-RMG 9229021 and 9220061).

Appendix A. Supplementary data

Supplementary data to this article can be found online at https://doi.org/10.1016/j.jcis.2025.01.201.

Data availability

Data will be made available on request.

References

[1] B. Jiang, J. Zhu, Z. Xia, J. Lyu, X. Li, L. Zheng, C. Chen, S. Chaemchuen, T. Bu, F. Verpoort, S. Mu, J. Wu, J. Wang, Z. Kou, Correlating single-atomic ruthenium interdistance with long-range interaction boosts hydrogen evolution reaction kinetics, Adv. Mater. 36 (2024) 2470009.
[2] P. Liu, X. Zhang, J. Fei, Y. Shi, J. Zhu, D. Zhang, L. Zhao, L. Wang, J. Lai, Frank partial dislocations in coplanar Ir/C ultrathin nanosheets boost hydrogen evolution reaction, Adv. Mater. 36 (2024) 2310591.
[3] D. Li, X. Xu, J. Jiang, H. Dong, H. Li, X. Peng, P.K. Chu, Coupled electrocatalytic hydrogen production, Mat. Sci. Eng. R 160 (2024) 100829.
[4] Q. Qian, Y. Zhu, N. Ahmad, Y. Feng, H. Zhang, M. Cheng, H. Liu, C. Xiao, G. Zhang, Y. Xie, Recent advancements in electrochemical hydrogen production via hybrid water splitting, Adv. Mater. 36 (2024) 2306108.
[5] Z.-Y. Yu, Y. Duan, X.-Y. Feng, X. Yu, M.-R. Gao, S.-H. Yu, Clean and affordable hydrogen fuel from alkaline water splitting: Past, recent progress, and future prospects, Adv. Mater. 33 (2021) 2007100.
[6] X. Li, L. Zhao, J. Yu, X. Liu, X. Zhang, H. Liu, W. Zhou, Water splitting: From electrode to green energy system, Nano-Micro Lett. 12 (2020) 131.
[7] Y. Mu, R. Ma, S. Xue, H. Shang, W. Lu, L. Jiao, Recent advances and perspective on transition metal heterogeneous catalysts for efficient electrochemical water splitting, Carbon Neutralization 3 (2024) 4–31.
[8] S. Xie, H. Dong, E.I. Iwuoha, X. Peng, Phase transition of catalysts for advanced electrocatalysis, Coord. Chem. Rev. 514 (2024) 215920.
[9] A. Hanan, M.N. Lakhan, F. Bibi, A. Khan, I.A. Soomro, A. Hussain, U. Aftab, MOFs coupled transition metals, graphene, and MXenes: Emerging electrocatalysts for hydrogen evolution reaction, Chem. Eng. J. 482 (2024) 148776.
[10] S. Feng, D. Li, H. Dong, S. Xie, Y. Miao, X. Zhang, B. Gao, P.K. Chu, X. Peng, Tailoring the Mo-N/Mo-O configuration in MoO_2/Mo_2N heterostructure for ampere-level current density hydrogen production, Appl. Catal. B-Environ. 342 (2024) 123451.
[11] S. Xie, C. Huang, H. Dong, B. Xu, Y. Miao, B. Gao, X. Zhang, P.K. Chu, X. Peng, A $MoNi_4$(312) surface preferred reconstruction enhancing hydrogen evolution, Appl. Catal. B-Environ. Energy 363 (2025) 124831.
[12] M. Batool, A. Hameed, M.A. Nadeem, Recent developments on iron and nickel-based transition metal nitrides for overall water splitting: A critical review, Coord. Chem. Rev. 480 (2023) 215029.

[13] X. Peng, C. Pi, X. Zhang, S. Li, K. Huo, P.K. Chu, Recent progress of transition metal nitrides for efficient electrocatalytic water splitting, Sustain. Energ. Fuels 3 (2019) 366–381.
[14] B. Ouyang, Y. Zhang, X. Wang, Y. Deng, F. Liu, Z. Fang, R.S. Rawat, E. Kan, Facet control of nickel nitride nano-framework for efficient hydrogen evolution electrocatalysis via auxiliary cooling assisted plasma engineering, Small 18 (2022) 2204634.
[15] Z. Qi, Y. Zeng, Z. Hou, W. Zhu, B. Wei, Y. Yang, B. Lin, H. Liang, Heterointerface engineering of Ni/Ni_3N hierarchical nanoarrays for efficient alkaline hydrogen evolution, Nano Res. 16 (2023) 4803–4811.
[16] H. Wang, J. Li, K. Li, Y. Lin, J. Chen, L. Gao, V. Nicolosi, X. Xiao, J.-M. Lee, Transition metal nitrides for electrochemical energy applications, Chem. Soc. Rev. 50 (2021) 1354–1390.
[17] B. Liu, B. He, H.Q. Peng, Y. Zhao, J. Cheng, J. Xia, J. Shen, T.W. Ng, X. Meng, C. S. Lee, W. Zhang, Unconventional nickel nitride enriched with nitrogen vacancies as a high-efficiency electrocatalyst for hydrogen evolution, Adv. Sci. 5 (2018) 1800406.
[18] Y. Ma, S. Lu, G. Han, Y. Liu, Z. Chen, Chemical vapor deposition of two-dimensional molybdenum nitride/graphene van der Waals heterostructure with enhanced electrocatalytic hydrogen evolution performance, Appl. Surf. Sci. 589 (2022) 152934.
[19] J. Xiong, W. Cai, W. Shi, X. Zhang, J. Li, Z. Yang, L. Feng, H. Cheng, Salt-templated synthesis of defect-rich MoN nanosheets for boosted hydrogen evolution reaction, J. Mater. Chem. A 5 (2017) 24193–24198.
[20] Y. Huang, W. Zhou, W. Kong, L. Chen, X. Lu, H. Cai, Y. Yuan, L. Zhao, Y. Jiang, H. Li, L. Wang, L. Wang, H. Wang, J. Zhang, J. Gu, Z. Fan, Atomically interfacial engineering on molybdenum nitride quantum dots decorated N-doped graphene for high-rate and stable alkaline hydrogen production, Adv. Sci. 9 (2022) 2204949.
[21] X. Liu, Z. Fang, X. Teng, Y. Niu, S. Gong, W. Chen, T.J. Meyer, Z. Chen, Paired formate and H_2 productions via efficient bifunctional Ni-Mo nitride nanowire electrocatalysts, J. Energy Chem. 72 (2022) 432–441.
[22] Y. Zhou, B. Chu, Z. Sun, L. Dong, F. Wang, B. Li, M. Fan, Z. Chen, Surface reconstruction and charge distribution enabling Ni/W_5N_4 Mott-Schottky heterojunction bifunctional electrocatalyst for efficient urea-assisted water electrolysis at a large current density, Appl. Catal. B-Environ. 323 (2023) 122168.
[23] B. Wang, L. Guo, J. Zhang, Y. Qiao, M. He, Q. Jiang, Y. Zhao, X. Shi, F. Zhang, Synthesis of nickel nitride-based 1D/0D heterostructure via a morphology-inherited nitridation strategy for efficient electrocatalytic hydrogen evolution, Small 18 (2022) 2201927.
[24] H. Yu, S. Zhu, Y. Hao, Y.-M. Chang, L. Li, J. Ma, H.-Y. Chen, M. Shao, S. Peng, Modulating local interfacial bonding environment of heterostructures for energy-saving hydrogen production at high current densities, Adv. Funct. Mater. 33 (2023) 2212811.
[25] X. Wang, X. Xu, Y. Nie, R. Wang, J. Zou, Electronic-state modulation of metallic co-assisted Co_7Fe_3 alloy heterostructure for highly efficient and stable overall water splitting, Adv. Sci. 10 (2023) 2301961.
[26] B.-C. Xu, Y.-P. Miao, M.-Q. Mao, D.-L. Li, S. Xie, W.-H. Jin, S. Xiao, J. Wen, Z. Abd-Allah, Z.-T. Liu, X. Peng, P.K. Chu, Heterophase junction engineering-induced Co spin-state modulation of $CoSe_2$ for large-current hydrogen evolution reaction, Rare Met. 43 (2024) 2660–2670.
[27] C. Zhu, A.-L. Wang, W. Xiao, D. Chao, X. Zhang, N.H. Tiep, S. Chen, J. Kang, X. Wang, J. Ding, J. Wang, H. Zhang, H.J. Fan, In situ grown epitaxial heterojunction exhibits high-performance electrocatalytic water splitting, Adv. Mater. 30 (2018) 1705516.
[28] B. Wang, F. Yang, L. Feng, Recent advances in Co-based electrocatalysts for hydrogen evolution reaction, Small 19 (2023) 2302866.
[29] Y. Zhang, Y. Ma, W. Yuan, L. Cai, Y. Chai, B. Qiu, Symmetry or asymmetry: Which one is the platform of nitrogen vacancies for alkaline hydrogen evolution, Mater. Horiz. 10 (2023) 4480–4487.
[30] J. Sun, W. Xu, C. Lv, L. Zhang, M. Shakouri, Y. Peng, Q. Wang, X. Yang, D. Yuan, M. Huang, Y. Hu, D. Yang, L. Zhang, Co/MoN hetero-interface nanoflake array with enhanced water dissociation capability achieves the Pt-like hydrogen evolution catalytic performance, Appl. Catal. B-Environ. 286 (2021) 119882.
[31] F. Lin, Z. Dong, Y. Yao, L. Yang, F. Fang, L. Jiao, Electrocatalytic hydrogen evolution of ultrathin Co-Mo_5N_6 heterojunction with interfacial electron redistribution, Adv. Energy Mater. 10 (2020) 2002176.
[32] B. Zhang, L. Zhang, Q. Tan, J. Wang, J. Liu, H. Wan, L. Miao, J. Jiang, Simultaneous interfacial chemistry and inner Helmholtz plane regulation for superior alkaline hydrogen evolution, Energy Environ. Sci. 13 (2020) 3007–3013.
[33] F. Song, W. Li, J. Yang, G. Han, P. Liao, Y. Sun, Interfacing nickel nitride and nickel boosts both electrocatalytic hydrogen evolution and oxidation reactions, Nat. Commun. 9 (2018) 4531.
[34] L. Zhao, L. Wei, H. He, X. Zhang, S. Liu, J. Wang, N-doped CoMo MOFs-derived carbon nanospheres electrocatalyst with Co/Mo-N bonds as bimetallic active sites for efficient hydrogen evolution reaction, Int. J. Hydrogen Energ. 62 (2024) 119–126.
[35] J. Ekspong, E. Gracia-Espino, T. Wågberg, Hydrogen evolution reaction activity of heterogeneous materials: A theoretical model, J. Phys. Chem. C 124 (2020) 20911–20921.
[36] W. Peng, Z. Wang, R. Lu, Q. Li, Z. Wang, Y. Zhao, L. Xu, L. Mai, Artificial heterointerfaces of defect-rich Ni and amorphous/crystalline MoN enable efficient hydrogen evolution reaction, Chem. Eng. J. 457 (2023) 141173.
[37] H. Sun, Z. Yan, F. Liu, W. Xu, F. Cheng, J. Chen, Self-supported transition-metal-based electrocatalysts for hydrogen and oxygen evolution, Adv. Mater. 32 (2020) 1806326.
[38] L. Wu, F. Zhang, S. Song, M. Ning, Q. Zhu, J. Zhou, G. Gao, Z. Chen, Q. Zhou, X. Xing, T. Tong, Y. Yao, J. Bao, L. Yu, S. Chen, Z. Ren, Efficient alkalinewater/seawater hydrogen evolution by a nanorod-nanoparticle-structured Ni-MoN catalyst with fast water-dissociation kinetics, Adv. Mater. 34 (2022) 2201774.
[39] J.K. Nørskov, T. Bligaard, A. Logadottir, J.R. Kitchin, J.G. Chen, S. Pandelov, U. Stimming, Trends in the exchange current for hydrogen evolution, J. Electrochem. Soc. 152 (2005) J23.
[40] L. Xiong, Y. Qiu, H. Dong, B. Gao, X. Zhang, P.K. Chu, X. Peng, Metallic Ni_3N/Ni heterostructure for efficient hydrogen evolution reaction, Int. J. Hydrogen Energ. 59 (2024) 400–407.
[41] X. Gao, X. Liu, W. Zang, H. Dong, Y. Pang, Z. Kou, P. Wang, Z. Pan, S. Wei, S. Mu, J. Wang, Synergizing in-grown Ni_3N/Ni heterostructured core and ultrathin Ni_3N surface shell enables self-adaptive surface reconfiguration and efficient oxygen evolution reaction, Nano Energy 78 (2020) 105355.
[42] Y. Liao, R. He, W. Pan, Y. Li, Y. Wang, J. Li, Y. Li, Lattice distortion induced Ce-doped NiFe-LDH for efficient oxygen evolution, Chem. Eng. J. 464 (2023) 142669.
[43] Y. Xu, M. Liu, S. Wang, K. Ren, M. Wang, Z. Wang, X. Li, L. Wang, H. Wang, Integrating electrocatalytic hydrogen generation with selective oxidation of glycerol to formate over bifunctional nitrogen-doped carbon coated nickel-molybdenum-nitrogen nanowire arrays, Appl. Catal. B-Environ. 298 (2021) 120493.
[44] L. Shang, Y. Zhao, X.-Y. Kong, R. Shi, G.I.N. Waterhouse, L. Wen, T. Zhang, Underwater superaerophobic Ni nanoparticle-decorated nickel-molybdenum nitride nanowire arrays for hydrogen evolution in neutral media, Nano Energy 78 (2020) 105375.
[45] L. Xiong, Y. Qiu, X. Peng, Z. Liu, P.K. Chu, Electronic structural engineering of transition metal-based electrocatalysts for the hydrogen evolution reaction, Nano Energy 104 (2022) 107882.
[46] C. Koventhan, A.-Y. Lo, Morphology engineering of novel $MnMoO_4$@$NiMoO_4$ core-shell nanostructure as an electrode material for asymmetric supercapacitor device, Chem. Eng. J. 485 (2024) 149950.
[47] S.H. Park, T.H. Jo, M.H. Lee, K. Kawashima, C.B. Mullins, H.-K. Lim, D.H. Youn, Highly active and stable nickel-molybdenum nitride (Ni_2Mo_3N) electrocatalyst for hydrogen evolution, J. Mater. Chem. A 9 (2021) 4945–4951.
[48] R.-Q. Li, X.-Y. Wan, B.-L. Chen, R.-Y. Cao, Q.-H. Ji, J. Deng, K.-G. Qu, X.-B. Wang, Y.-C. Zhu, Hierarchical Ni_3N/$Ni_{0.2}Mo_{0.8}N$ heterostructure nanorods arrays as efficient electrocatalysts for overall water and urea electrolysis, Chem. Eng. J. 409 (2021) 128240.
[49] Y. Chen, Y. Wang, J. Yu, G. Xiong, H. Niu, Y. Li, D. Sun, X. Zhang, H. Liu, W. Zhou, Underfocus laser induced Ni nanoparticles embedded metallic MoN microrods as patterned electrode for efficient overall water splitting, Adv. Sci. 9 (2022) 2105869.
[50] M. Ning, Y. Wang, L. Wu, L. Yang, Z. Chen, S. Song, Y. Yao, J. Bao, S. Chen, Z. Ren, Hierarchical interconnected NiMoN with large specific surface area and high mechanical strength for efficient and stable alkaline water/seawater hydrogen evolution, Nano-Micro Lett. 15 (2023) 157.
[51] Y. Li, Y. Jiao, H. Yan, G. Yang, Y. Liu, C. Tian, A. Wu, H. Fu, Mo-Ni-based heterojunction with fine-customized d-band centers for hydrogen production coupled with benzylamine electrooxidation in low alkaline medium, Angew. Chem. Int. Ed. 62 (2023) e202306640.
[52] P. Wang, J. Bai, B. Zhao, H. Ma, W. Li, X. Zhu, Y. Sun, Intercalation reaction in amorphous layer-wrapped $Ni_{0.2}Mo_{0.8}N$/Ni_3N heterostructure toward efficient lithium-Ion storage, ACS Appl. Mater. Interfaces 14 (2022) 38875–38886.
[53] C. Huang, M. Feng, Y. Peng, B. Zhang, J. Huang, X. Yue, S. Huang, In situ construction of Ni/$Ni_{0.2}Mo_{0.8}N$ heterostructure to enhance the alkaline hydrogen oxidation reaction by balancing the binding of intermediates, Adv. Funct. Mater. 33 (2023) 2300593.
[54] H. Wang, W. Fu, X. Yang, Z. Huang, J. Li, H. Zhang, Y. Wang, Recent advancements in heterostructured interface engineering for hydrogen evolution reaction electrocatalysis, J. Mater. Chem. A 8 (2020) 6926–6956.
[55] W. Hua, H. Sun, H. Liu, Y. Li, J.-G. Wang, Interface engineered NiMoN/Ni_3N heterostructures for enhanced alkaline hydrogen evolution reaction, Appl. Surf. Sci. 540 (2021) 148407.
[56] M. Arabi, A. Ghaffarinejad, G.B. Darband, Electrodeposition of nanoporous nickel selenide on graphite rod as a bifunctional electrocatalyst for hydrogen and oxygen evolution reactions, J. Electroanal. Chem. 907 (2022) 116066.
[57] W. Mu, D. Bao, C. Chang, Growth of nickel vacancy NiFe-LDHs on $Ni(OH)_2$ nanosheets as highly efficient bifunctional electrocatalyst for overall water splitting, Int. J. Hydrogen Energ. 47 (2022) 15603–15611.
[58] J. Wang, M. Zhang, G. Yang, W. Song, W. Zhong, X. Wang, M. Wang, T. Sun, Y. Tang, Heterogeneous bimetallic Mo-NiP_x/NiS_y as a highly efficient electrocatalyst for robust overall water splitting, Adv. Funct. Mater. 31 (2021) 2101532.
[59] A. Ali, P. Chen, Q.U. Khan, P.K. Shen, A novel in-situ strategy develops for Mo_2C nanoparticles incorporated on N, P co-doped stereotaxically carbon as efficient electrocatalyst for overall water splitting, Int. J. Hydrogen Energ. 47 (2022) 15969–15981.
[60] A. Wu, Y. Gu, Y. Xie, H. Yan, Y. Jiao, D. Wang, C. Tian, Interfacial engineering of MoS_2/MoN heterostructures as efficient electrocatalyst for pH-universal hydrogen evolution reaction, J. Alloys Compd. 867 (2021) 159066.
[61] Y. Ling, F.M.D. Kazim, Q. Zhang, S. Xiao, M. Li, Z. Yang, Construction of Mo_2C/W_2C heterogeneous electrocatalyst for efficient hydrogen evolution reaction, Int. J. Hydrogen Energ. 46 (2021) 9699–9706.
[62] C.J. Oluigbo, Y. Xu, H. Louis, A.B. Yusuf, W. Yaseen, N. Ullah, K.J. Alagarasan, M. Xie, E.E. Ekpenyong, J. Xie, Controllable fabrication of abundant nickel-

nitrogen doped CNT electrocatalyst for robust hydrogen evolution reaction, Appl. Surf. Sci. 562 (2021) 150161.
[63] A. Saad, Y. Gao, K.A. Owusu, W. Liu, Y. Wu, A. Ramiere, H. Guo, P. Tsiakaras, X. Cai, Ternary Mo_2NiB_2 as a superior bifunctional electrocatalyst for overall water splitting, Small 18 (2022) 2104303.
[64] D. Guo, Z. Wan, G. Fang, M. Zhu, B. Xi, A tandem interfaced (Ni_3S_2-MoS_2)@TiO_2 composite fabricated by atomic layer deposition as efficient HER electrocatalyst, Small 18 (2022) 2201896.
[65] X. Fang, L. Ren, F. Li, Z. Jiang, Z.-G. Wang, Modulating electronic structure of $CoSe_2$ by Ni doping for efficient electrocatalyst for hydrogen evolution reaction, Rare Met. 41 (2021) 901–910.
[66] X. Zhang, T. Liu, T. Guo, Z. Mu, X. Hu, K. He, X. Chen, V.P. Dravid, Z. Wu, D. Wang, High-performance MoC electrocatalyst for hydrogen evolution reaction enabled by surface sulfur substitution, ACS Appl. Mater. Interfaces 13 (2021) 40705–40712.
[67] X. Yang, W. Yang, X. Fu, J. Hu, J. Chen, N-enriched porous carbon doped with Co, Ni, and Mo as efficient electrocatalyst for hydrogen evolution reaction, Int. J. Hydrogen Energ. 46 (2021) 18318–18325.
[68] C. Chen, N. Suo, X. Han, X. He, Z. Dou, Z. Lin, L. Cui, Tuning the morphology and electron structure of metal-organic framework-74 as bifunctional electrocatalyst for OER and HER using bimetallic collaboration strategy, J. Alloys Compd. 865 (2021) 158795.
[69] K. Song, H. Zhang, Z. Lin, Z. Wang, L. Zhang, X. Shi, S. Shen, S. Chen, W. Zhong, Interfacial engineering of cobalt thiophosphate with strain effect and modulated electron structure for boosting electrocatalytic hydrogen evolution reaction, Adv. Funct. Mater. 34 (2024) 2312672.
[70] Z. Wang, S. Shen, J. Wang, W. Zhong, Modulating the d-band center of electrocatalysts for enhanced water splitting, Chem.-Eur. J. (2024) e202402725.
[71] Z. Sun, B. Chu, S. Wang, L. Dong, Q. Pang, M. Fan, X. Zhang, H. He, B. Li, Z. Chen, Hydrogen-bond induced and hetero coupling dual effects in N-doped carbon coated CrN/Ni nanosheets for efficient alkaline freshwater/seawater hydrogen evolution, J. Colloid Interf. Sci. 646 (2023) 361–369.

Enhancing hydrogen evolution by heterointerface engineering of Ni/MoN catalysts

Junzheng Jiang[1], Yunfan Qiu[1], Hao Dong[1], Lei Yang[2], Yaping Miao[3], Liwei Xiong[1], Biao Gao[4], Xuming Zhang[4], Paul K. Chu[5], Xiang Peng[1]*

[1] Hubei Key Laboratory of Plasma Chemistry and Advanced Materials, Engineering Research Center of Phosphorus Resources Development and Utilization of Ministry of Education, School of Materials Science and Engineering, Wuhan Institute of Technology, Wuhan 430205, China

[2] Research Center for Monitoring and Environmental Sciences, Taihu Basin & East China Sea Ecological Environment Supervision and Administration Authority, Ministry of Ecology and Environment, Shanghai 200125, China

[3] School of Textile Science and Engineering, Xi'an Polytechnic University, Xi'an 710048, China

[4] The State Key Laboratory of Refractories and Metallurgy, Institute of Advanced Materials and Nanotechnology, Wuhan University of Science and Technology, Wuhan 430081, China

[5] Department of Physics, Department of Materials Science and Engineering, and Department of Biomedical Engineering, City University of Hong Kong, Tat Chee Avenue, Kowloon, Hong Kong, China

* Correspondence: xpeng@wit.edu.cn (X. Peng)

TOF calculation

To calculate the per-site TOF, we use the following formula:

$$TOF = \frac{number\ of\ total\ hydrogen\ turnovers/cm^2}{number\ of\ active\ of\ sites/cm^2}\ .$$

The total number of hydrogen turnovers is calculated from the current density according to:

$$No.of\ H_2 = \left(j\frac{mA}{cm^2}\right)\left(\frac{1\ C\ s^{-1}}{1000\ mA}\right)\left(\frac{1\ mol\ e^{-1}}{96485.3\ C}\right)\left(\frac{1\ mol\ H_2}{2\ mol\ e^{-1}}\right)\left(\frac{6.022\times10^{23} H_2\ mulecules}{1\ mol\ H_2}\right) =$$

$$3.12\times10^{15}\frac{H_2\ s^{-1}}{cm^2}per\frac{mA}{cm^2}.$$

The active sites per real surface area are calculated by the following formula:

$$No.of\ active\ sites = \left(\frac{No.of\ atoms/unit\ cell}{Volunme/unit\ cell}\right)^{\frac{2}{3}}.$$

Therefore, the number of active sites of Ni/MoN/CC is derived by the following formula:

$$No.of\ active\ sites\times ECSA = \left(\frac{No.of\ atoms/unit\ cell}{Volume/unit\ cell}\right)^{\frac{2}{3}}\times x\times ECSA +$$

$$\left(\frac{No.of\ atoms/unit\ cell}{Volume/unit\ cell}\right)^{\frac{2}{3}}\times y\times ECSA,$$

where x and y are the molar ratios of MoN and Ni at the surface of Ni/MoN. MoN contains two Mo atoms and two N atoms with a volume of 160.1 Å^3 and Ni contains four Ni atoms with a volume of 43.8 Å^3. The phase ratio of MoN to Ni is determined by XPS using XPSPEAK. Ni/MoN contains 63.9% MoN and 36.1% Ni.

MoN

$$No.of\ active\ sites = \left(\frac{No.of\ atoms/unit\ cell}{Volunme/unit\ cell}\right)^{\frac{2}{3}}$$

$$No.of\ active\ sites = \left(\frac{4\ atoms/unit\ cell}{160.1\ Å^3/unit\ cell}\right)^{\frac{2}{3}}$$

$$No.of\ active\ sites = 2.498\times10^{14}\ atoms\ cm^{-2}$$

$$ECSA = \frac{Specific\ capacitance\ (\mu F\ cm^{-2})}{40\ \mu F\ cm^{-2}\ per\ cm^2_{ECSA}} = A_{geo} \times \frac{17900\ (\mu F\ cm^{-2})}{40\ \mu F\ cm^{-2}}$$

$$TOF = \frac{(3.12 \times 10^{15}\ \frac{H_2\ s^{-1}}{cm^2}\ per\ \frac{mA}{cm^2}) \times |j|}{no.of\ active\ sites\ \times ECSA}$$

Metallic Ni

$$No.of\ active\ sites = \left(\frac{No.of\ atoms/unit\ cell}{Volunme/unit\ cell}\right)^{\frac{2}{3}}$$

$$No.of\ active\ sites\ = \left(\frac{4\ atoms/unit\ cell}{43.8\ Å^3/unit\ cell}\right)^{\frac{2}{3}}$$

$$No.of\ active\ sites = 9.132 \times 10^{14}\ atoms\ cm^{-2}$$

$$ECSA = \frac{Specific\ capacitance\ (\mu F\ cm^{-2})}{40\ \mu F\ cm^{-2}\ per\ cm^2_{ECSA}} = A_{geo} \times \frac{2800\ (\mu F\ cm^{-2})}{40\ \mu F\ cm^{-2}}$$

$$TOF = \frac{(3.12 \times 10^{15}\ \frac{H_2\ s^{-1}}{cm^2}\ per\ \frac{mA}{cm^2}) \times |j|}{no.of\ active\ sites\ \times ECSA}$$

Ni/MoN

$$No.of\ active\ sites = \left(\frac{No.of\ atoms/unit\ cell}{Volunme/unit\ cell}\right)^{\frac{2}{3}}$$

$$No.of\ active\ sites\ (\mathrm{MoN}) = \left(\frac{4\ atoms/unit\ cell}{160.1\ Å^3/unit\ cell}\right)^{\frac{2}{3}}$$

$$No.of\ active\ sites = 2.498 \times 10^{14}\ atoms\ cm^{-2}$$

$$No.of\ active\ sites\ (\mathrm{Mo_2N}) = \left(\frac{4\ atoms/unit\ cell}{43.8\ Å^3/unit\ cell}\right)^{\frac{2}{3}}$$

$$No.of\ active\ sites = 9.132 \times 10^{14}\ atoms\ cm^{-2}$$

$$ECSA = \frac{Specific\ capacitance\ (\mu F\ cm^{-2})}{40\ \mu F\ cm^{-2}\ per\ cm^2_{ECSA}} = A_{geo} \times \frac{25500\ (\mu F\ cm^{-2})}{40\ \mu F\ cm^{-2}}$$

$$TOF = \frac{(3.12 \times 10^{15}\ \frac{H_2\ s^{-1}}{cm^2}\ per\ \frac{mA}{cm^2}) \times |j|}{no.of\ active\ sites\ (MoN) \times x \times ECSA + no.of\ active\ sites\ (Ni) \times y \times ECSA}$$

where x = 63.9% and y = 36.1%.

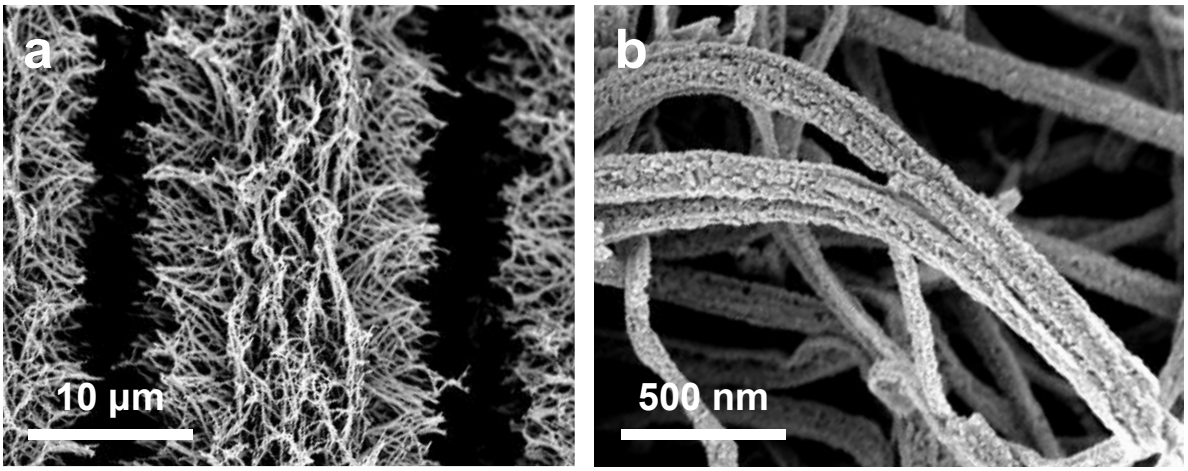

Figure S1. (a-b) SEM images of MoN/CC.

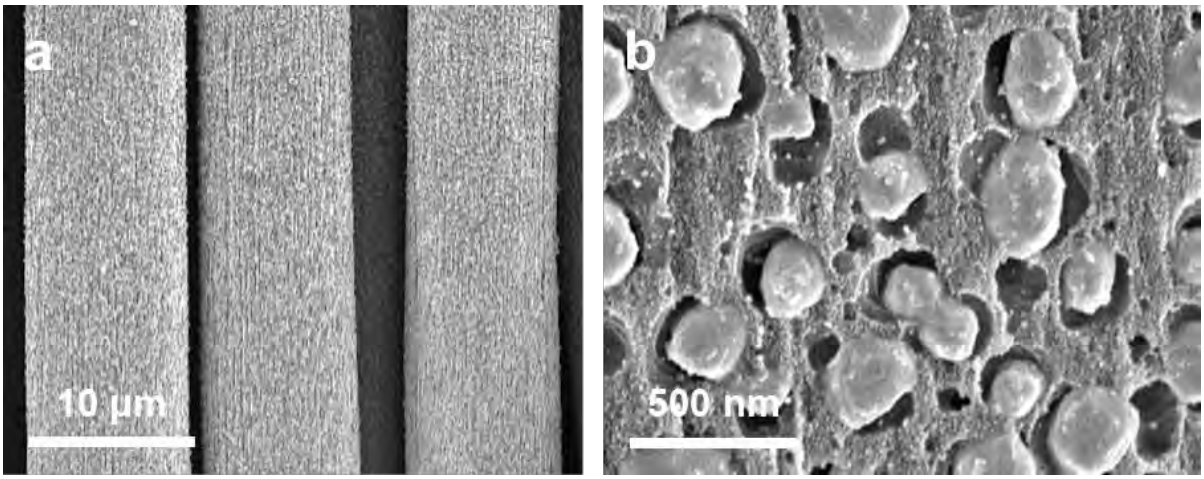

Figure S2. (a-b) SEM images of Ni/CC.

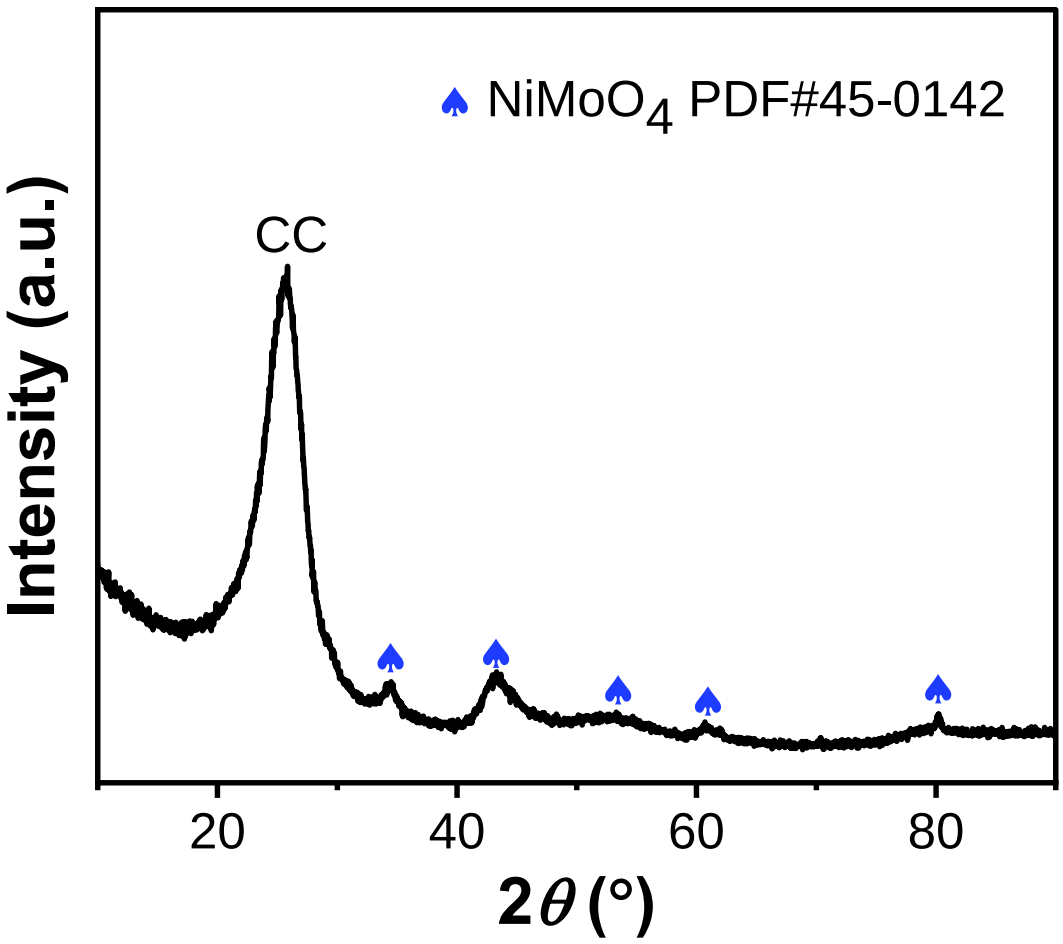

Figure S3. XRD pattern of $NiMoO_4$/CC.

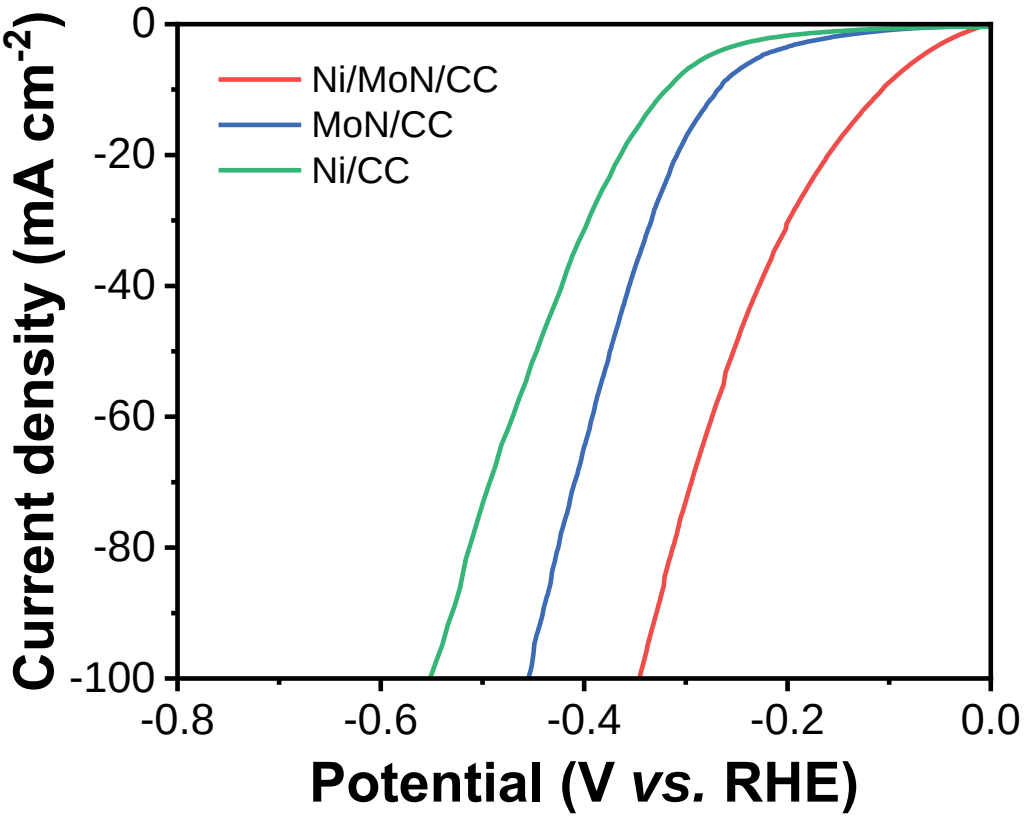

Figure S4. The uncorrected polarization curves of Ni/MoN/CC, MoN/CC, and Ni/CC.

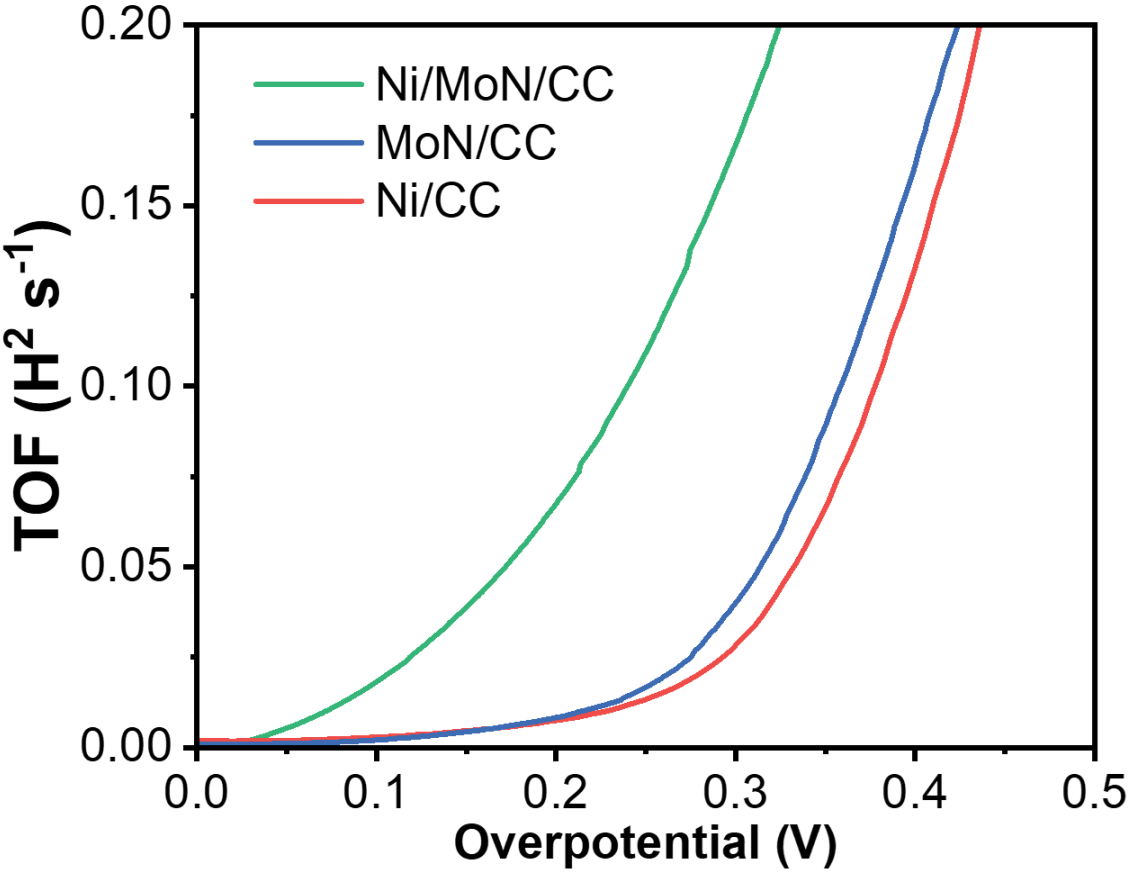

Figure S5. TOF of Ni/MoN/CC、MoN/CC and Ni/CC.

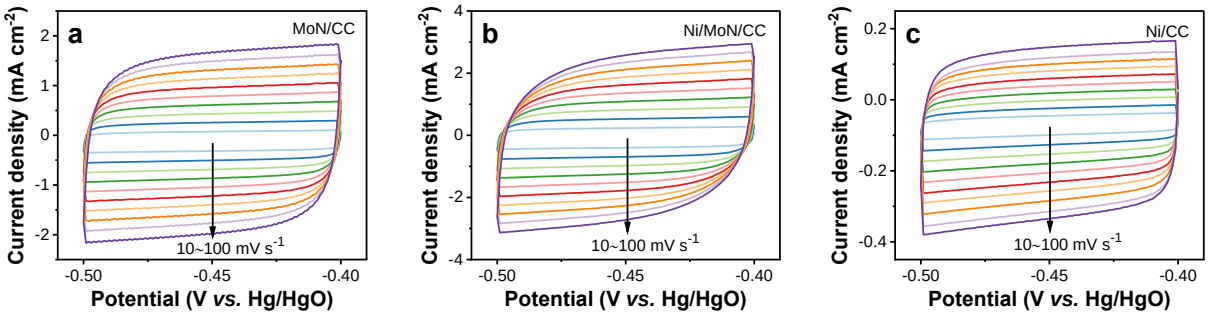

Figure S6. CV curves of (a) MoN/CC, (b) Ni/MoN/CC, and (c) Ni/CC.

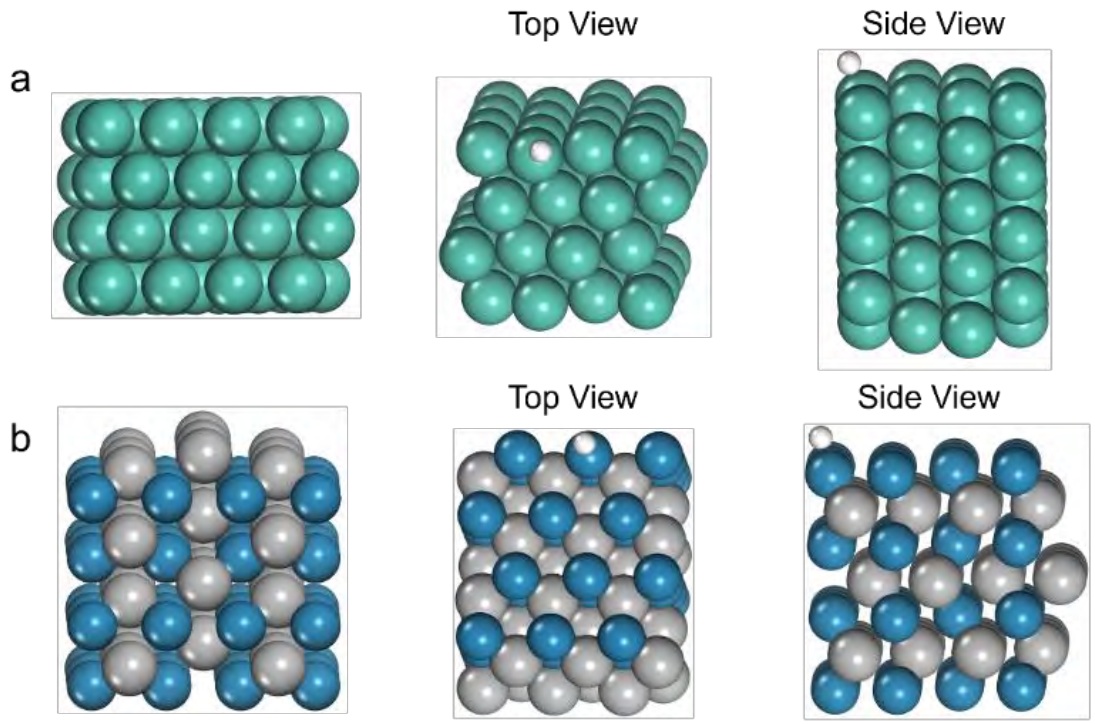

Figure S7. Models for (a) Ni(111) surface and (b) MoN(200) surface along with hydrogen adsorption.